Main Manuscript for

Force and step size of gliding motility in human pathogenic bacterium *Mycoplasma pneumoniae*

Masaki Mizutani[a,1], Yuya Sasajima[a], Makoto Miyata[a,b*]

[a]Graduate School of Science, Osaka City University, 3-3-138 Sugimoto, Sumiyoshi-ku, Osaka 558-8585, Japan
[b]The OCU Advanced Research Institute for Natural Science and Technology (OCARINA), Osaka City University, 3-3-138 Sugimoto, Sumiyoshi-ku, Osaka 558-8585, Japan

*Makoto Miyata

Email: miyata@osaka-cu.ac.jp

For proper authentication, authors must provide their ORCID at submission and are not permitted to add ORCIDs to the proofs.

Masaki Mizutani: https://orcid.org/0000-0001-7950-4866

Yuya Sasajima: https://orcid.org/0000-0002-5942-2625

Makoto Miyata: https://orcid.org/0000-0002-7478-7390

Author Contributions: M. Mizutani designed the study. M. Mizutani and Y.S. analyzed the genomes. M Mizutani performed all other experiments. M. Mizutani and M. Miyata wrote the paper, and all the authors completed it.

Competing Interest Statement: The authors declare no competing interest.

Classification: Biological Sciences, Microbiology.

Keywords: Motility, Optical tweezers, class *Mollicutes*, Infection.

Abstract

Mycoplasma pneumoniae, a human pathogenic bacterium, binds to sialylated oligosaccharides and glides on host cell surfaces via a unique mechanism. Gliding motility is essential for initiating the infectious process. In the present study, we measured the stall force of an *M. pneumoniae* cell carrying a bead that was manipulated using optical tweezers on two strains. The stall forces of M129 and FH strains were averaged to be 23.7 and 19.7 pN, respectively, much weaker than those of other bacterial surface motilities. The binding activity and gliding speed on sialylated oligosaccharides of the M129 strain were eight and two times higher than those of the FH strain, respectively, showing that binding activity is not linked to gliding force. Gliding speed decreased when cell binding was reduced by addition of free sialylated oligosaccharides, indicating the existence of a drag force during gliding. We detected stepwise movements under 0.2–0.3 mM free sialylated oligosaccharides. A step size of 14–19 nm showed that 25–35 propulsion steps per second are required to achieve the usual gliding speed. The step size was reduced to less than half with the load applied using optical tweezers, showing that a 2.5 pN force from a cell is exerted on a leg. The work performed in this step was 16–30% of the free energy of the hydrolysis of ATP molecules, suggesting that this step is linked to the elementary process of *M. pneumoniae* gliding.

Significance Statement

Human mycoplasma pneumonia is caused by the bacterium *Mycoplasma pneumoniae*. This tiny bacterium, shaped like a missile, binds to human epithelial surfaces and spreads using a unique gliding mechanism to establish infection. Here, we analyzed the movements and force of this motility using a special setup: optical tweezers. We then obtained detailed mechanical data to understand this mechanism. Furthermore, we succeeded in detecting small steps of nanometers in its gliding, which is likely linked to the elementary process of the core reaction: chemical to mechanical energy conversion. These data provide critical information to both control this human pathogen and explore new ideas for artificial molecular machines.

Introduction

Members of the bacterial class *Mollicutes*, which includes the genus *Mycoplasma*, are parasitic and occasionally commensal bacteria that are characterized by small cells and genomes and by the absence of a peptidoglycan layer (1, 2). *Mycoplasma* species bind to host cell surfaces and exhibit gliding motility to spread the infectious area. Interestingly, *Mycoplasma* gliding does not involve flagella or pili and is completely unrelated to other bacterial motility systems or conventional motor proteins that are common in eukaryotic motility (3). The gliding motility of *Mycoplasma* is divided into two types, *Mycoplasma pneumoniae* and *Mycoplasma mobile* types, which share no homology in component proteins, indicating independent mechanisms (4, 5).

M. pneumoniae is a human pathogen that causes respiratory diseases, including bronchitis and atypical pneumonia (6). *M. pneumoniae* cells bind to human epithelial surfaces through sialylated oligosaccharides (SOs), which are major structures of animal

cell surfaces related to cell-cell recognition, and the binding targets of many pathogens and toxins (7-10). The cells show unidirectional gliding motility at a speed of up to 1 μm/s on SOs-coated glass surfaces (Fig. 1A) (5, 11), which is known to be essential for their infection (12). The gliding machinery, called the "attachment organelle," is localized at a cell pole (13). The attachment organelle is divided into two parts: internal and surface structures. The internal structure is composed of an internal core complex and a surrounding translucent area. The internal core comprises three parts: a terminal button, paired plates, and a bowl complex from the front side of the cell (Fig. 1B) (5, 14, 15). The major surface structure, called "P1 adhesin complex" or "genitalium and pneumoniae cytoadhesin (GPCA)", is composed of P1 adhesin and P40/P90 proteins and aligned around the internal structure, which plays a dual role as the adhesin to bind to SOs and as the leg for gliding (Fig. 1B) (16-20). The model for gliding called the "Inchworm model" or "Double-spring hybrid ratchet model" is proposed, in which cells repeat the extensions and contractions of the attachment organelle based on the energy from ATP hydrolysis to enable smooth gliding (15, 21-23). Generally, the mechanical characteristics and detailed analysis of movements are essential for creating and completing a detailed model for the motility mechanism. However, to date, no information is available about the force for gliding.

In the present study, we measured the stall forces of the two strains and discuss the relationship between binding and force. Furthermore, we succeeded in detecting and measuring stepwise movements that are likely linked to the elementary process of the gliding reaction.

Results

Stall force measurement using optical tweezers

Optical tweezers are commonly used to measure the stall force generated by pili in bacterial motility or motor proteins in eukaryotic motility (24-27). The stall force is defined as the force needed to stop movements and is equal to the maximal propulsion force for locomotion. Previously, we measured the stall force for the gliding motility of *M. mobile*, based on a mechanism unrelated to *M. pneumoniae* gliding, using optical tweezers (28, 29). In the present study, we applied this method to *M. pneumoniae* gliding. *M. pneumoniae* cells were biotinylated and inserted into a tunnel chamber, which was assembled using two glass plates and double-sided tape (30). An avidin-conjugated polystyrene bead was trapped by a highly focused laser beam and attached to a gliding cell at the back end of the cell body by exploiting the avidin-biotin interaction. The cells pulled the bead from the trap center with gliding and then stalled (Fig. 2A and B; *SI Appendix*, Movie S1). The force was calculated by measuring the distance between the centers of the bead and the laser trap, which was multiplied by the trap stiffness; the force acting on the bead increased linearly with the displacement from the trap center (24). Starting from 0 s, the pulling force increased and reached a plateau in 120 s (Fig. 2C). The maximal value of the force averaged over one second was determined as the stall force. The stall force of M129 strain cells was 23.7 ± 6.3 pN (Fig. 2E). We also measured the stall force of the FH strain, another major strain of *M. pneumoniae*. The cells of the FH strain pulled the bead in a manner similar to that of M129 cells (*SI Appendix*, Movie S2). The stall force of the FH strain was 19.7 ± 5.3 pN, significantly weaker than that of the M129 strain (Fig. 2D and E).

108 **Binding activity and gliding motility**

109 To characterize the differences in gliding motility, we measured the binding activity and gliding
110 speed of the M129 and FH strains. *M. pneumoniae* cells were suspended in HEPES buffer
111 containing 20 mM glucose to obtain an optical density at 595 nm of 0.07, then inserted into tunnel
112 chambers. After incubation for 5–30 min, the tunnel chambers were washed and observed by
113 phase-contrast microscopy. The number of bound cells in the M129 strain increased with time
114 from 90 ± 16 to 308 ± 20 cells in 100 ×100 μm^2 area from 5 to 30 min (Fig. 3A and B). These
115 values are consistent with the results of previous report (9). In contrast, the number of bound cells
116 in the FH strain increased from 12 ± 2 to 36 ± 8 cells from 5 to 30 min (Fig. 3A and B). The
117 number of bound cells in the FH strain was 7.2–8.7-fold smaller than that of the M129 strain at all
118 time points (Fig. 3B). When 10× concentrated cell suspension was examined, the bound cell
119 numbers of the FH strain increased from 117 ± 10 to 386 ± 24 cells from 5 to 30 min, 1.2–1.3
120 times that of M129 at all time points (Fig. 3A and B). These results indicate that the FH strain has
121 approximately 8-fold lower binding activity to SOs-coated glass surfaces than the M129 strain.
122 Considering that the stall force of FH was only 1.2-fold smaller than that of the M129 strain, the
123 force is unlikely to be linked to binding activity.

124 Most of the bound cells showed gliding motility on the SOs-coated glass (Fig. 3C;
125 *SI Appendix*, Movies S3 and S4). To characterize gliding motility, the proportion of gliding
126 cells and gliding speed were analyzed. The proportion of gliding cells to all bound cells
127 was 78.1% (n_{total} = 2284, n_{glide} = 1785) and 60.0% (n_{total} = 2271, n_{glide} = 1362) in the M129
128 and FH strains, respectively (Fig. 3C). The gliding speeds averaged for 20 s at 1-s
129 intervals were 0.47 ± 0.08 and 0.21 ± 0.07 μm/s for M129 and FH strains, respectively
130 (Fig. 3D). These results suggest that binding activity is not directly linked to gliding speed.

131

132 **Differences in amino acid sequences of gliding proteins between two strains**

133 The FH strain used in this study has not been genomically analyzed. Therefore, we sequenced
134 the genomes of both strains using MiSeq (*SI Appendix*, Dataset S1) and analyzed the sequences
135 of 14 genes that have been reported to be involved in binding and gliding (5). Only one amino
136 acid was substituted in the M129 strain genome from a standard genome, M129-B7 (GenBank
137 accession no. CP003913), which was V196A in the HMW3 protein, which is positioned at the
138 terminal button in the attachment organelle (Fig. 1B). Our FH strain had 161 and 155 variations
139 from the reported FH and FH2009 strains, respectively (GenBank accession no. CP010546 and
140 CP017327), indicating that the FH strain is distant from the genome strains. The differences
141 between the two strains analyzed in the present study in terms of the 14 genes were as follows:
142 (i) P1 adhesin showed many differences, including 87 single amino acid substitutions, 18 amino
143 acid insertions, and four amino acid deletions, known differences of FH from M129 strains (*SI*
144 *Appendix*, Fig. S1). (ii) The P40/P90 protein showed 96 single amino acid substitutions, one
145 amino acid insertion, and 68 amino acid deletions (*SI Appendix*, Fig. S2). (iii) The other 12 genes
146 showed 0–5 mutations in each gene, as summarized in *SI Appendix*, Table S1.

147

148 **Effect of free sialyllactose on binding and gliding**

149 *M. pneumoniae* cells have hundreds of legs and glide smoothly on solid surfaces. To trace the
150 behavior of a single propulsion event, the number of working legs should be reduced by adding a
151 free form of SO, which is the binding target for gliding (9, 29, 31). To quantitatively analyze the
152 effects of free SO on the binding activity and gliding under our conditions, we measured the
153 bound ratio of cells and the gliding speed of the M129 strain under various concentrations of the
154 SO 3'-*N*-acetylneuraminyllactose (SL). *M. pneumoniae* cells suspended in the buffer were
155 inserted into a tunnel chamber. Then, the cell behavior in 0–0.5 mMSL solutions was analyzed.
156 The addition of free SL slowed down and then stopped gliding or released the gliding cells from
157 the glass surfaces, but did not release non-gliding cells, indicating that release requires glass
158 binding by GPCA with displacements (Fig. 4A). The number of gliding cells and the gliding speed
159 relative to the initial speed were decreased by 0.1–0.5 mM with SL treatments from 55 ± 11% to
160 26 ± 16% and from 0.33 ± 0.06 to 0.19 ± 0.07 μm/s, respectively (Fig. 4B and C). We then
161 decided to use 0.2–0.3 mM concentrations for further experiments because the binding and
162 gliding were partially inhibited under these conditions, which were advantageous for observing
163 single propulsion events during gliding.

164

165 **Stepwise gliding movements observed under free SL**

166 Next, we traced cells under 0.2–0.3 mM free SL conditions as performed in the stall force
167 measurements. The gliding cells slowly pulled the beads from the trap center. Half of the tested
168 cells stalled in 120 s, but the other cells repeated creeping movements and detachment from the
169 glass surfaces (Fig. 5A). The stall force of the cells that reached a plateau in 120 s was 16.2 ± 4.5
170 pN (Fig. 5B), which was significantly weaker than that without SL ($p = 1.1\times10^{-5}$ by Student's *t*-
171 test). In creeping movements, cells occasionally showed discontinuous displacements, which
172 were mostly stepwise (Fig. 5C and D). Individual displacements in a stepwise time course were
173 analyzed using the pairwise distance function (29, 31). The displacements shown in Fig. 5D were
174 uniformly distributed at about 17-, 14-, and 16-nm intervals under 0.15, 0.20, and 0.17 pN/nm of
175 trap stiffness, corresponding to 2.55, 2.80, and 2.66 pN of propulsion force, respectively (Fig. 5D
176 and E). Note that force increments are generally calculated from the trap stiffness × displacement
177 (24, 29).

178 Next, to examine the load dependency of step sizes in detail, we measured step sizes
179 under 0.07–0.26 pN/nm of trap stiffness. Ninety-seven steps in 36 cell trajectories, including at
180 least two continuous steps, were detected. The step sizes under 0.13 to 0.26 pN/nm of trap
181 stiffness linearly decreased from 21.0 to 8.0 nm with trap stiffness (Fig. 5F and H). In contrast, the
182 step sizes from 0.07 to 0.12 pN/nm of trap stiffness were mostly constant and distributed at 14–
183 19 nm with an average of 16.2 ± 2.7 nm ($n = 21$) (Fig. 5G–I).

184 From 0.07 to 0.12 pN/nm of trap stiffness, the force increments increased with the trap
185 stiffness (Fig. 5I). In the cases where the force values increase with trap stiffness, the calculated
186 force does not reflect the actual force because the load is too small to influence the movements.
187 Therefore, we focused on the force increments measured under 0.13–0.26 pN/nm of trap
188 stiffness. The force exerted in a single propulsion step was concluded to be 2.5 ± 0.3 pN ($n = 76$)
189 (Fig. 5J).

190

Discussion

M. pneumoniae has weak stall force

In the present study, we measured the stall force in *M. pneumoniae* gliding using optical tweezers. Previously, the stall force was measured for some bacterial surface motilities. *Neisseria gonorrhoeae* and *Myxococcus xanthus* show surface motility driven by the retraction of type IV pili (32). The stall forces of single-pilus retraction in *N. gonorrhoeae* and *M. xanthus* were measured by optical tweezers to be approximately 80 and 150 pN, respectively (25, 33). *M. mobile* glides up to 4.0 μm/s by a mechanism unrelated to that of *M. pneumoniae*. Previously, we measured the stall force of *M. mobile* gliding using optical tweezers to be approximately 113 pN (23). The stall forces of *M. pneumoniae* gliding were 23.7 ± 6.3 and 19.7 ± 5.3 pN in M129 and FH strains, respectively (Fig. 2E), much weaker than those of other bacterial surface motilities. *M. pneumoniae* has a streamlined cell body about 0.2 μm in a diameter (34). This shape and cell size may be beneficial for gliding in human tissues with weak forces.

In liquid culture, *M. pneumoniae* cells bind to the bottom surface of the tissue culture flask. This is distinct from the case of *M. mobile*, in which most cells float in the medium. Therefore, *M. pneumoniae* is expected to have a stronger force for gliding than *M. mobile*. However, we found that *M. pneumoniae* had a much weaker stall force than *M. mobile* (Fig. 2E). When comparing the two strains of *M. pneumoniae*, the FH strain showed much less active binding than, but a stall force comparable to, that of M129 (Fig. 2E and 3B). These facts indicate that the binding activity of *M. pneumoniae* cells is not determined by the gliding force, which is represented by the stall force.

Drag force in gliding

The gliding speed decreased when cell binding was partially inhibited by the addition of free SL (Fig. 4). This observation is consistent with previous data; that is, the inhibition of binding by monoclonal antibodies decreased the gliding speed of *M. pneumoniae* (35), and the inhibition by SL decreased the speed of *M. gallisepticum*, coinciding with the common mechanism with *M. pneumoniae* (23). The decrease in speed was probably caused by the drag force generated from the substrate surface, because the friction force exerted from water is estimated to be more than 5000 times smaller than the stall force of 24 pN (Fig. 2E) (36, 37). As the cause of the drag force, two possibilities are considered: GPCA and others. If some proportion of GPCA molecules are not involved in gliding, they are not released from SOs by inhibitory factors, resulting in speed reduction. Interestingly, these observations and explanations are similar to the case of *M. mobile* gliding, even though they do not share the same structure of machinery (4, 9, 37-39). This scheme may be advantageous for gliding on SOs based on ATP energy.

Stepwise movement as elementary process

We succeeded in detecting the stepwise movements of *M. pneumoniae* gliding. *M. pneumoniae* cells glided at a speed of 0.47 μm/s (Fig. 3D), and the step size in the load-free condition was 14–19 nm (Fig. 5I), suggesting 25–35 steps per second. Stepwise movements are well-studied in

231 ATP-driven eukaryotic motor proteins including myosin, dynein, and kinesin (40, 41). The force
232 and displacement of a single step in myosin II, cytoplasmic dynein, kinesin-1, and myosin V have
233 been reported as 3–5, 7–8, 8, and 2–3 pN and 5.3, 8, 8, and 36 nm, respectively (24, 26, 27, 42-
234 44). Stepwise movements are also present in bacterial motility. A flagellar motor shows 14
235 degrees of revolution as a step (45, 46). The gliding of *M. mobile* shows stepwise movements of
236 1.5 pN force and 70 nm length (29, 31). Generally, stepwise movements are thought to
237 correspond to the elementary process of a motility event.

238 Previously, we showed that *M. pneumoniae*-type gliding motility is driven by energy from
239 ATP hydrolysis (23). Motilities driven by ATP energy can be divided into elementary processes
240 that are directly coupled with ATP hydrolysis, such as stepwise movements. The elementary
241 processes observed as steps can use only smaller work than the energy produced by ATP
242 hydrolysis ~80 pN nm (47). Therefore, we estimated the work done in the stepwise movements of
243 *M. pneumoniae* gliding to determine this possibility. The work was estimated to be 18.2 ± 5.4 pN
244 nm from the equation Wstep = 0.5 × spring constant × displacement^2, under 0.13–0.26 pN/nm of
245 trap stiffness, where the stiffness is large enough to determine the force (*SI Appendix*, Fig. S3)
246 (29). This value is 16%–30% of the free energy of the hydrolysis of ATP molecules, suggesting
247 that we detected the elementary process of *M. pneumoniae* gliding. The energy conversion
248 efficiencies of stepwise movements are 12%–40%, 10%, and 40%–60% for myosin II,
249 cytoplasmic dynein, and kinesin, respectively (40, 41). Previously, we estimated it to be 10%–
250 40% for *M. mobile* gliding (29). These facts suggest that the energy efficiency of stepwise
251 movements of *M. pneumoniae* is in a similar range of myosin II and *M. mobile* gliding.

252

253 **Load-dependent step size**

254 *M. pneumoniae* cells showed different step sizes depending on the load provided by optical
255 tweezers continuously (Fig. 5I), suggesting that the step size of *M. pneumoniae* is load-
256 dependent. In the infectious process, *M. pneumoniae* cells glide to the deep positions of
257 respiratory systems and experience a large load at these positions (12). The load-dependent
258 stepping manner would be useful to glide against large loads because a load-independent
259 stepping motor, kinesin, shows frequent back steps under large loads (48, 49). Different step
260 sizes under different loads have also been observed in *M. mobile* gliding (29, 31).

261

262 **Suggestion for gliding mechanism**

263 How can we image the gliding mechanism? The GPCA probably plays a critical role in *M.*
264 *pneumoniae* gliding, because antibodies against the P1 adhesin, a component of GPCA,
265 decreased the gliding speed and ultimately replaced the *M. pneumoniae* cells on the glass
266 surface (35). Recently, the detailed structure of GPCA has been solved (17-20). It is a mushroom
267 structure composed of two P1 adhesins and two P40/P90 molecules. The C-terminal regions of
268 the four molecules are bundled and anchored to the cell membrane. P40 and P90 proteins are
269 synthesized as a single protein and processed into two proteins that are not observed in *M.*
270 *genitalium*. Although P1 adhesin is believed to be the receptor for SOs, the binding site exists at
271 the distal end of P40/P90. This complex is suggested to undergo conformational changes

272 between open and closed binding pockets, which are likely involved in the gliding mechanism (18,
273 20).

274 The attachment organelle responsible for gliding can be divided into a surface structure
275 including GPCA and an internal rod structure (15, 22, 50-52). Briefly, the force for gliding
276 is likely generated at the bowl because a few proteins essential for gliding and not binding
277 are localized there (53-55). The paired plates and elastic components play a role in force
278 transmission, because the gliding speed decreases seriously in a deletion mutant (56).
279 The terminal button likely connects the rod front to the cell membrane, because an end
280 component, the P30 protein, features transmembrane segments (57, 58).

281 Here, we focus on the following observations to construct the working model for
282 the gliding scheme: (1) The force is probably generated around the bowl complex,
283 transmits through the internal structures including paired plates, and reaches GPCAs. (2)
284 Inhibition of cell binding decreases gliding speed. (3) GPCA has open and closed
285 conformations. (4) Gliding can be divided into steps because binding and force are not
286 tightly coupled. (5) The gliding movement can be divided into 14–19 nm steps with a 2.5
287 pN force.

288

289 **Gliding scheme to explain stepwise movements**

290 The model is composed of repeated cycle of four stages (i)–(iv) connected by four steps: “Power
291 stroke,” “Release,” “Displacement,” and “Catch” (Fig. 6). (i) The GPCA in the open state catches
292 an SO on the glass surface. (ii) Contraction of the internal structure pulls the cell body with 2.5 pN
293 and a step size of 14–19 nm. This step is possibly linked to energy from an ATP molecule. (iii)
294 GPCA switches into a closed state by triggering the pulling force transmitted from other working
295 GPCAs, resulting in the release of after-stroke GPCA from the SO. (iv) The released GPCA
296 returns to the open state and displaces another SO in the next position by the extension of the
297 internal structure. (i) The GPCA captures the next SO. The full cycle was then repeated. This
298 scheme explains the relationship between the binding and force of different strains, if we assume
299 that release is enhanced and power stroke and catch are reduced in FH compared with those in
300 M129. The observation that shorter steps occur under load can be explained if we consider that
301 the power stroke is shortened by the load (Fig. 4I).

302 Previously, our group suggested a working model for *M. pneumoniae* gliding, focusing mainly on
303 the information of the internal structure with regard to the attachment organelle (Kawamoto. 2016.
304 mBio; Miyata. 2016. Front Micro). The previous model suggested “directed detachment of feet”
305 (GPCA), due to the lack of information about step, force, and foot structure. In this study, we
306 succeeded in adding new information and completing an updated model.
307

308 # Materials and Methods

309 **Strains and Cultivation**

310 *M. pneumoniae* M129 (ATCC29342) and FH strains were grown in SP-4 medium at 37 °C in
311 tissue culture flasks (TPP Techno Plastic Products AG, Trasadingen, Switzerland), as described

312 previously (11, 59). The FH strain was kindly provided by Tsuyoshi Kenri at the National Institute
313 of Infectious Diseases, Tokyo, Japan.

314

315 **Optical tweezers system**

316 An inverted microscope (IX71; Olympus, Tokyo, Japan) was equipped with a Nd:YAG laser
317 (ASF1JE01; Furukawa Electric, Tokyo, Japan) to construct the optical tweezers. The microscope
318 stage was replaced by a piezoelectric stage controlled by a stage controller (MDR14-CA-2.5;
319 SIGMAKOKI, Tokyo, Japan) and a joystick (JS-300; SIGMAKOKI). The irradiated laser beam was
320 concentrated as a finite optical system using a plano-convex lens supported by an optical cage
321 system (SIGMAKOKI). The concentrated laser beam was inserted into the microscope and
322 focused by an objective lens (CFI Apochromat TIRF 100XC Oil; Nikon, Tokyo, Japan). The actual
323 laser power was measured using a power meter (FieldMaxII; COHERENT, Santa Clara, CA)
324 without the objective lens.

325

326 **Force measurements**

327 The cell suspension was mixed with 0.5 mM Sulfo-NHS-LC-LC-biotin (Thermo Fisher Scientific,
328 Waltham, MA) as the final concentration and incubated for 15 min at room temperature (RT). The
329 cell suspension was centrifuged at 12,000 × *g* for 10 min, washed with 10 mM HEPES buffer (pH
330 7.4) containing 150 mM NaCl, centrifuged again, washed with HEPES buffer containing 10% non-
331 heat-inactivated horse serum (Gibco; Thermo Fisher Scientific) and 20 mM glucose, passed
332 through a 0.45-μm pore size filter and incubated for 15 min at RT. The cell suspension was
333 inserted into a tunnel chamber, which was assembled by taping coverslips cleaned with saturated
334 ethanolic KOH and precoated with 100% non-heat-inactivated horse serum for 60 min and 10
335 mg/ml bovine serum albumin (Sigma-Aldrich, St. Louis, MO) in HEPES buffer for 60 min at RT.
336 The tunnel chamber was washed with HEPES buffer containing 20 mM glucose and incubated at
337 37 °C on optical tweezers equipped with a thermo plate (MATS-OTOR-MV; Tokai Hit, Shizuoka,
338 Japan) and a lens heater (MATS-LH; Tokai Hit). Avidin-conjugated beads in the HEPES buffer
339 containing 20 mM glucose and 0.2–0.3 mM of 3'-*N*-acetylneuraminyllactose (SL) were sonicated
340 and inserted into the tunnel chamber. The avidin-conjugated beads were prepared as previously
341 described (30). The bead movements were recorded using a charge-coupled device (CCD)
342 camera (LRH2500XE-1; DigiMo, Tokyo, Japan) at 30 frames per second and analyzed by
343 displacement of up to 200 nm from the trap center (the linear range of the laser trap) using
344 ImageJ 1.43u (http://rsb.info.nih.gov/ij/) and IGOR Pro 6.33 J and 8.02 J (WaveMetrics, Portland,
345 OR) (29, 30, 60).

346

347 **Binding and gliding analyses**

348 Cultured cells were washed with buffer in a culture flask, and then washed with HEPES buffer
349 containing 10% non-heat-inactivated horse serum (Gibco™; Thermo Fisher Scientific, Waltham,
350 MA) and 20 mM glucose. Cultured cells were scraped off the culture flask, passed through a
351 0.45-μm pore size filter, and incubated for 15 min at RT. The cell suspension was then inserted

352 into the tunnel chamber. The tunnel chamber was washed with HEPES buffer containing 20 mM
353 glucose, incubated at 37 °C on an inverted microscope (IX83; Olympus) equipped with a thermo
354 plate and lens heater, observed by phase-contrast microscopy at 37 °C, and recorded with a
355 CCD camera (DMK 33UX174; The Imaging Source Asia Co. Ltd., Taiepi City, Taiwan). Then, the
356 tunnel chamber was washed with HEPES buffer containing 20 mM glucose and various
357 concentrations of SL. Video data were analyzed using ImageJ 1.43u and IGOR Pro 6.33 J.

358

359 **Genome sequencing and variant analyses**

360 Frozen stocks of cells were plated on Aluotto medium and isolated as previously described (61).
361 Genomic DNA was isolated and sequenced using MiSeq (Illumina, San Diego, CA), as previously
362 described (29). Sequence read mapping and variant detection were performed using the CLC
363 Genomics Workbench (QIAGEN, Hilden, Germany).

364 Acknowledgments

365 We thank Dr. Tsuyoshi Kenri at the National Institute of Infectious Diseases and Dr. Ikuko
366 Fujiwara at Osaka City University for helpful discussions, and Dr. Shigeyuki Kakizawa at the
367 National Institute of Advanced Industrial Science and Technology (AIST) for supporting the
368 genome sequence analyses. This work was supported by Grants-in-Aid for Scientific Research:
369 (A) (MEXT KAKENHI Grant Numbers JP24390107, JP17H01544) and by JST CREST (Grant
370 Number JPMJCR19S5, Japan). M. Mizutani is the recipient of a Research Fellowship of the
371 Japan Society for the Promotion of Science (18J15362).

372 References

373 1. S. Razin, D. Yogev, Y. Naot, Molecular biology and pathogenicity of mycoplasmas.
374 *Microbiol Mol Biol Rev* **62**, 1094-1156 (1998).
375 2. S. Razin, L. Hayflick, Highlights of mycoplasma research--an historical perspective.
376 *Biologicals* **38**, 183-190 (2010).
377 3. M. Miyata *et al.*, Tree of motility - A proposed history of motility systems in the tree of life.
378 *Genes Cells* **25**, 6-21 (2020).
379 4. M. Miyata, T. Hamaguchi, Prospects for the gliding mechanism of *Mycoplasma mobile*.
380 *Curr Opin Microbiol* **29**, 15-21 (2016).
381 5. M. Miyata, T. Hamaguchi, Integrated information and prospects for gliding mechanism of
382 the pathogenic bacterium *Mycoplasma pneumoniae*. *Front Microbiol* **7**, 960 (2016).
383 6. T. Saraya, *Mycoplasma pneumoniae* infection: Basics. *J Gen Fam Med* **18**, 118-125
384 (2017).
385 7. R. Nagai, M. Miyata, Gliding motility of *Mycoplasma mobile* can occur by repeated
386 binding to *N*-acetylneuraminyllactose (sialyllactose) fixed on solid surfaces. *J Bacteriol*
387 **188**, 6469-6475 (2006).
388 8. A. Varki, Sialic acids in human health and disease. *Trends Mol Med* **14**, 351-360 (2008).
389 9. T. Kasai *et al.*, Role of binding in *Mycoplasma mobile* and *Mycoplasma pneumoniae*
390 gliding analyzed through inhibition by synthesized sialylated compounds. *J Bacteriol* **195**,
391 429-435 (2013).
392 10. C. R. Williams *et al.*, Sialylated receptor setting influences *Mycoplasma pneumoniae*
393 attachment and gliding motility. *Mol Microbiol* **109**, 735-744 (2018).
394 11. D. Nakane, M. Miyata, Cytoskeletal asymmetrical dumbbell structure of a gliding
395 mycoplasma, *Mycoplasma gallisepticum*, revealed by negative-staining electron

396 microscopy. *J Bacteriol* **191**, 3256-3264 (2009).
397 12. O. A. Prince, T. M. Krunkosky, D. C. Krause, In vitro spatial and temporal analysis of
398 *Mycoplasma pneumoniae* colonization of human airway epithelium. *Infect Immun* **82**,
399 579-586 (2014).
400 13. S. Seto, G. Layh-Schmitt, T. Kenri, M. Miyata, Visualization of the attachment organelle
401 and cytadherence proteins of *Mycoplasma pneumoniae* by immunofluorescence
402 microscopy. *J Bacteriol* **183**, 1621-1630 (2001).
403 14. D. Nakane, T. Kenri, L. Matsuo, M. Miyata, Systematic structural analyses of attachment
404 organelle in *Mycoplasma pneumoniae*. *PLoS Pathog* **11**, e1005299 (2015).
405 15. A. Kawamoto *et al.*, Periodicity in attachment organelle revealed by electron
406 cryotomography suggests conformational changes in gliding mechanism of *Mycoplasma*
407 *pneumoniae*. *MBio* **7**, e00243-00216 (2016).
408 16. D. Nakane, J. Adan-Kubo, T. Kenri, M. Miyata, Isolation and characterization of P1
409 adhesin, a leg protein of the gliding bacterium *Mycoplasma pneumoniae*. *J Bacteriol* **193**,
410 715-722 (2011).
411 17. D. Aparicio *et al.*, *Mycoplasma genitalium* adhesin P110 binds sialic-acid human
412 receptors. *Nat Commun* **9**, 4471 (2018).
413 18. D. Aparicio *et al.*, Structure and mechanism of the Nap adhesion complex from the
414 human pathogen *Mycoplasma genitalium*. *Nat Commun* **11**, 2877 (2020).
415 19. D. Vizarraga *et al.*, Immunodominant proteins P1 and P40/P90 from human pathogen
416 *Mycoplasma pneumoniae*. *Nat Commun* **11**, 5188 (2020).
417 20. D. Vizarraga, S. Torres-Puig, D. Aparicio, O. Q. Pich, The sialoglycan binding adhesins of
418 *Mycoplasma genitalium* and *Mycoplasma pneumoniae*. *Trends Microbiol* **29**, 477-481
419 (2021).
420 21. M. Miyata, Centipede and inchworm models to explain *Mycoplasma* gliding. *Trends*
421 *Microbiol* **16**, 6-12 (2008).
422 22. A. Seybert *et al.*, Cryo-electron tomography analyses of terminal organelle mutants
423 suggest the motility mechanism of *Mycoplasma genitalium*. *Mol Microbiol* **108**, 319-329
424 (2018).
425 23. M. Mizutani, M. Miyata, Behaviors and energy source of *Mycoplasma gallisepticum*
426 gliding. *J Bacteriol* **201**, e00397-00319 (2019).
427 24. H. Kojima, E. Muto, H. Higuchi, T. Yanagida, Mechanics of single kinesin molecules
428 measured by optical trapping nanometry. *Biophys J* **73**, 2012-2022 (1997).
429 25. A. J. Merz, M. So, M. P. Sheetz, Pilus retraction powers bacterial twitching motility. *Nature*
430 **407**, 98-102 (2000).
431 26. Y. Takagi, E. E. Homsher, Y. E. Goldman, H. Shuman, Force generation in single
432 conventional actomyosin complexes under high dynamic load. *Biophys J* **90**, 1295-1307
433 (2006).
434 27. A. Gennerich, A. P. Carter, S. L. Reck-Peterson, R. D. Vale, Force-induced bidirectional
435 stepping of cytoplasmic dynein. *Cell* **131**, 952-965 (2007).
436 28. M. Miyata, W. S. Ryu, H. C. Berg, Force and velocity of *Mycoplasma mobile* gliding. *J*
437 *Bacteriol* **184**, 1827-1831 (2002).
438 29. M. Mizutani, I. Tulum, Y. Kinosita, T. Nishizaka, M. Miyata, Detailed analyses of stall force
439 generation in *Mycoplasma mobile* gliding. *Biophys J* **114**, 1411-1419 (2018).
440 30. M. Mizutani, M. Miyata, Force measurement on *Mycoplasma mobile* gliding using optical
441 tweezers. *Bio Protoc* **7**, e2127 (2017).
442 31. Y. Kinosita *et al.*, Unitary step of gliding machinery in *Mycoplasma mobile*. *Proc. Natl.*
443 *Acad. Sci. USA* **111**, 8601-8606 (2014).
444 32. V. Pelicic, Type IV pili: *e pluribus unum*? *Mol Microbiol* **68**, 827-837 (2008).
445 33. M. Clausen, V. Jakovljevic, L. Sogaard-Andersen, B. Maier, High-force generation is a
446 conserved property of type IV pilus systems. *J Bacteriol* **191**, 4633-4638 (2009).
447 34. J. M. Hatchel, M. F. Balish, Attachment organelle ultrastructure correlates with phylogeny,
448 not gliding motility properties, in *Mycoplasma pneumoniae* relatives. *Microbiology* **154**,
449 286-295 (2008).

35. S. Seto, T. Kenri, T. Tomiyama, M. Miyata, Involvement of P1 adhesin in gliding motility of *Mycoplasma pneumoniae* as revealed by the inhibitory effects of antibody under optimized gliding conditions. *J Bacteriol* **187**, 1875-1877 (2005).
36. R. Rosengarten, M. Fischer, H. Kirchhoff, G. Kerlen, K. H. Seack, Transport of erythrocytes by gliding cells of *Mycoplasma mobile* 163K. *Current Microbiology* **16**, 253-257 (1988).
37. A. Uenoyama, A. Kusumoto, M. Miyata, Identification of a 349-kilodalton protein (Gli349) responsible for cytadherence and glass binding during gliding of *Mycoplasma mobile*. *J Bacteriol* **186**, 1537-1545 (2004).
38. A. Uenoyama, S. Seto, D. Nakane, M. Miyata, Regions on Gli349 and Gli521 protein molecules directly involved in movements of *Mycoplasma mobile* gliding machinery, suggested by use of inhibitory antibodies and mutants. *J Bacteriol* **191**, 1982-1985 (2009).
39. M. S. Nishikawa *et al.*, *Mycoplasma mobile* gliding based on structure, ATPase activity, and sialic acid binding of machinery. *MBio* **10**, e02846-02819 (2019).
40. C. Bustamante, Y. R. Chemla, N. R. Forde, D. Izhaky, Mechanical processes in biochemistry. *Annu Rev Biochem* **73**, 705-748 (2004).
41. R. Mallik, B. C. Carter, S. A. Lex, S. J. King, S. P. Gross, Cytoplasmic dynein functions as a gear in response to load. *Nature* **427**, 649-652 (2004).
42. M. J. Schnitzer, S. M. Block, Kinesin hydrolyses one ATP per 8-nm step. *Nature* **388**, 386-390 (1997).
43. K. Fujita, M. Iwaki, A. H. Iwane, L. Marcucci, T. Yanagida, Switching of myosin-V motion between the lever-arm swing and brownian search-and-catch. *Nat Commun* **3**, 956 (2012).
44. P. J. Park, K. J. Lee, A modified active Brownian dynamics model using asymmetric energy conversion and its application to the molecular motor system. *J Biol Phys* **39**, 439-452 (2013).
45. Y. Sowa *et al.*, Direct observation of steps in rotation of the bacterial flagellar motor. *Nature* **437**, 916-919 (2005).
46. S. Nakamura, N. Kami-ike, J. P. Yokota, T. Minamino, K. Namba, Evidence for symmetry in the elementary process of bidirectional torque generation by the bacterial flagellar motor. *Proc Natl Acad Sci U S A* **107**, 17616-17620 (2010).
47. R. Yasuda, H. Noji, K. Kinosita, Jr., M. Yoshida, F_1-ATPase is a highly efficient molecular motor that rotates with discrete 120 degree steps. *Cell* **93**, 1117-1124 (1998).
48. N. J. Carter, R. A. Cross, Kinesin's moonwalk. *Current opinion in cell biology* **18**, 61-67 (2006).
49. A. Toleikis, N. J. Carter, R. A. Cross, Backstepping mechanism of kinesin-1. *Biophys J* **119**, 1984-1994 (2020).
50. G. P. Henderson, G. J. Jensen, Three-dimensional structure of *Mycoplasma pneumoniae*'s attachment organelle and a model for its role in gliding motility. *Mol Microbiol* **60**, 376-385 (2006).
51. A. Seybert, R. Herrmann, A. S. Frangakis, Structural analysis of *Mycoplasma pneumoniae* by cryo-electron tomography. *J Struct Biol* **156**, 342-354 (2006).
52. D. C. Krause *et al.*, Electron cryotomography of *Mycoplasma pneumoniae* mutants correlates terminal organelle architectural features and function. *Mol Microbiol* **108**, 306-318 (2018).
53. B. M. Hasselbring, J. L. Jordan, D. C. Krause, Mutant analysis reveals a specific requirement for protein P30 in *Mycoplasma pneumoniae* gliding motility. *J Bacteriol* **187**, 6281-6289 (2005).
54. J. L. Jordan *et al.*, Protein P200 is dispensable for *Mycoplasma pneumoniae* hemadsorption but not gliding motility or colonization of differentiated bronchial epithelium. *Infect Immun* **75**, 518-522 (2007).
55. Y. Kawakita *et al.*, Structural study of MPN387, an essential protein for gliding motility of a human-pathogenic bacterium, *Mycoplasma pneumoniae*. *J Bacteriol* **198**, 2352-2359

(2016).
56. L. Garcia-Morales, L. Gonzalez-Gonzalez, E. Querol, J. Pinol, A minimized motile machinery for *Mycoplasma genitalium*. *Mol Microbiol* **100**, 125-138 (2016).
57. H. Y. Chang, J. L. Jordan, D. C. Krause, Domain analysis of protein P30 in *Mycoplasma pneumoniae* cytadherence and gliding motility. *J Bacteriol* **193**, 1726-1733 (2011).
58. R. F. Relich, M. F. Balish, Insights into the function of *Mycoplasma pneumoniae* protein P30 from orthologous gene replacement. *Microbiology (Reading)* **157**, 2862-2870 (2011).
59. J. G. Tully, New laboratory techniques for isolation of *Mycoplasma pneumoniae*. *Yale J Biol Med* **56**, 511-515 (1983).
60. A. Tanaka, D. Nakane, M. Mizutani, T. Nishizaka, M. Miyata, Directed binding of gliding bacterium, *Mycoplasma mobile*, shown by detachment force and bond lifetime. *MBio* **7**, e00455-00416 (2016).
61. I. Tulum, M. Yabe, A. Uenoyama, M. Miyata, Localization of P42 and F_1-ATPase alpha-subunit homolog of the gliding machinery in *Mycoplasma mobile* revealed by newly developed gene manipulation and fluorescent protein tagging. *J Bacteriol* **196**, 1815-1824 (2014).

522 # Figures

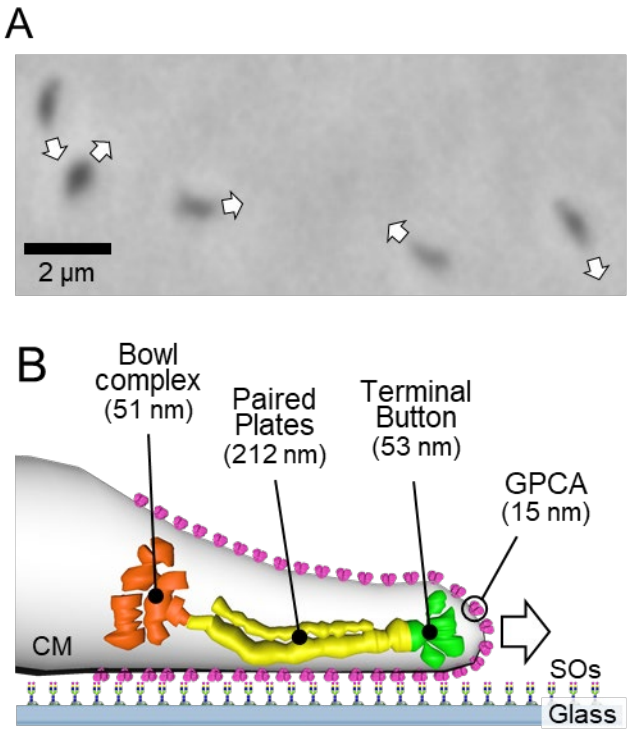

523
524
525 **Figure 1. Gliding motility of *Mycoplasma pneumoniae*.** (A) Phase-contrast micrograph of *M.*
526 *pneumoniae* cells. The gliding directions of cells are indicated by white arrows. (B) Illustration of
527 gliding machinery. The gliding machinery is composed of the bowl complex, paired plates,
528 terminal button, and GPCA. The lengths along the cell axis are summarized from previous studies
529 (14, 19). GPCA, working as a leg, is anchored to the cell membrane (CM) and catches sialylated
530 oligosaccharides (SOs) fixed on solid surfaces.
531
532

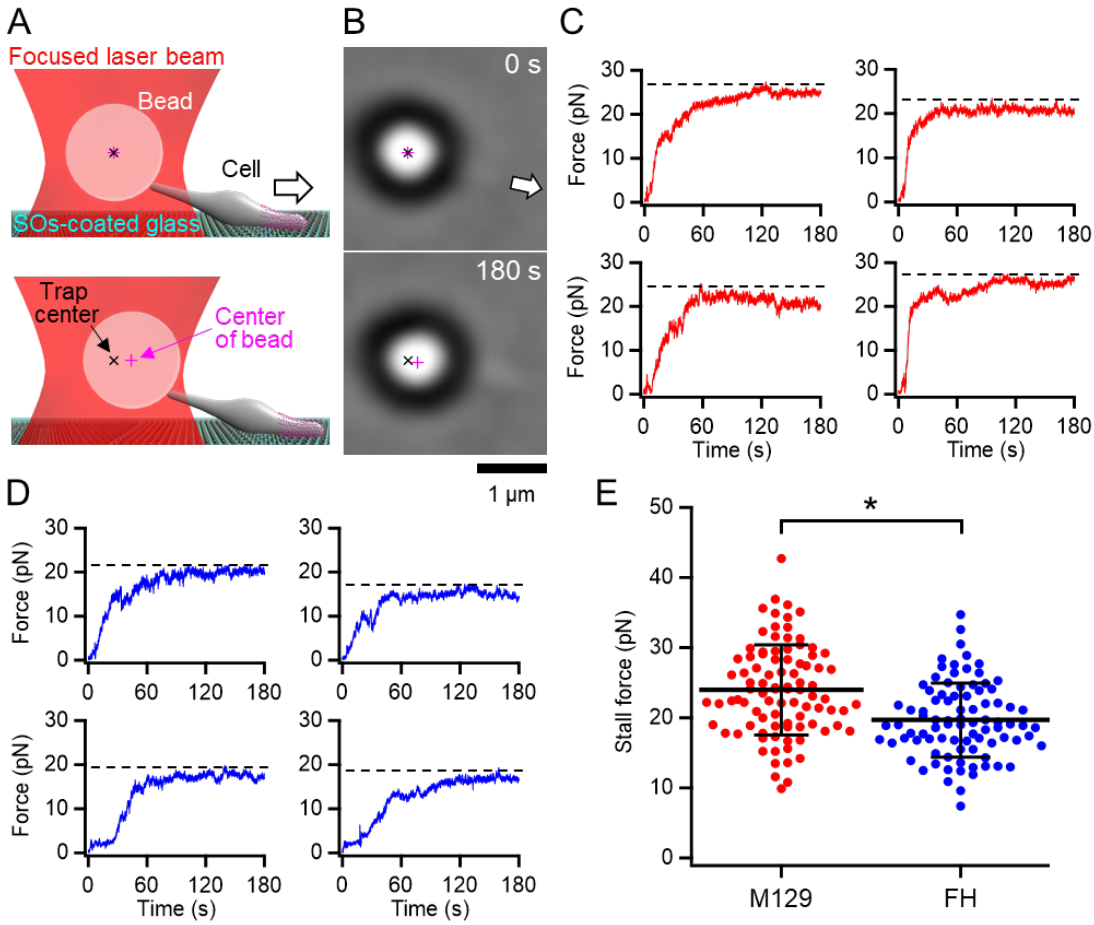

Figure 2. Stall force measurements. (A) Illustrations of experimental design for force measurements. The white arrow indicates the gliding direction. (B) Optical micrographs of a trapped cell. The cell attached with a bead (large black ring with white center) glided in the direction of the white arrow from 0 and stalled in 180 s. The cell image can be observed near the base of the arrow. (C) Four representative time courses of force increments for M129 strain. The broken lines indicate the values of stall force. (D) Four representative time courses of force increments for FH strain. The broken lines indicate the values of stall force. (E) Scatter dot plot of stall force (n = 92 and 88 in M129 and FH, respectively) shown with averages (thick lines) and standard deviations (thin lines). *$p = 2.4\times10^{-6}$ by Student's t-test.

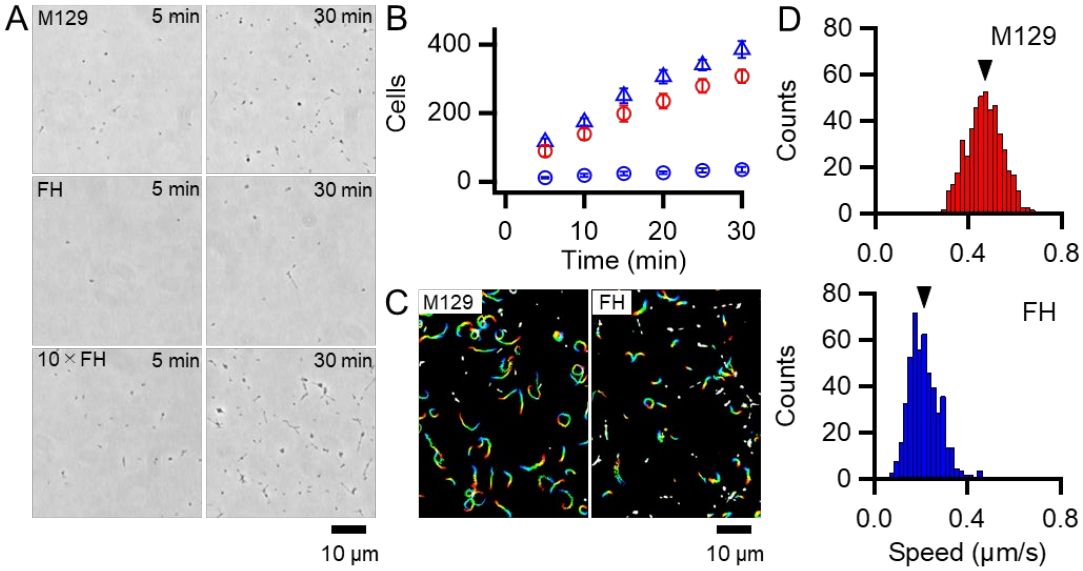

Figure 3. Binding activity and gliding motility. (A) Phase-contrast micrographs of cells on SO-coated glass surfaces. M129, FH, and 10× concentrated FH are shown after 5 and 30 min of incubation. (B) Averaged bound cell numbers in 100×100 μm^2 plotted with standard deviations (n = 10 in each). M129 (red open circle), FH (blue open circle), and 10× concentrated FH (blue open triangle) are presented. (C) Cell trajectories for 20 s, changing color with time from red to blue. (D) Distributions of gliding speeds averaged for 20 s at 1-s intervals (n = 500 in each). Mean values are marked by black triangles.

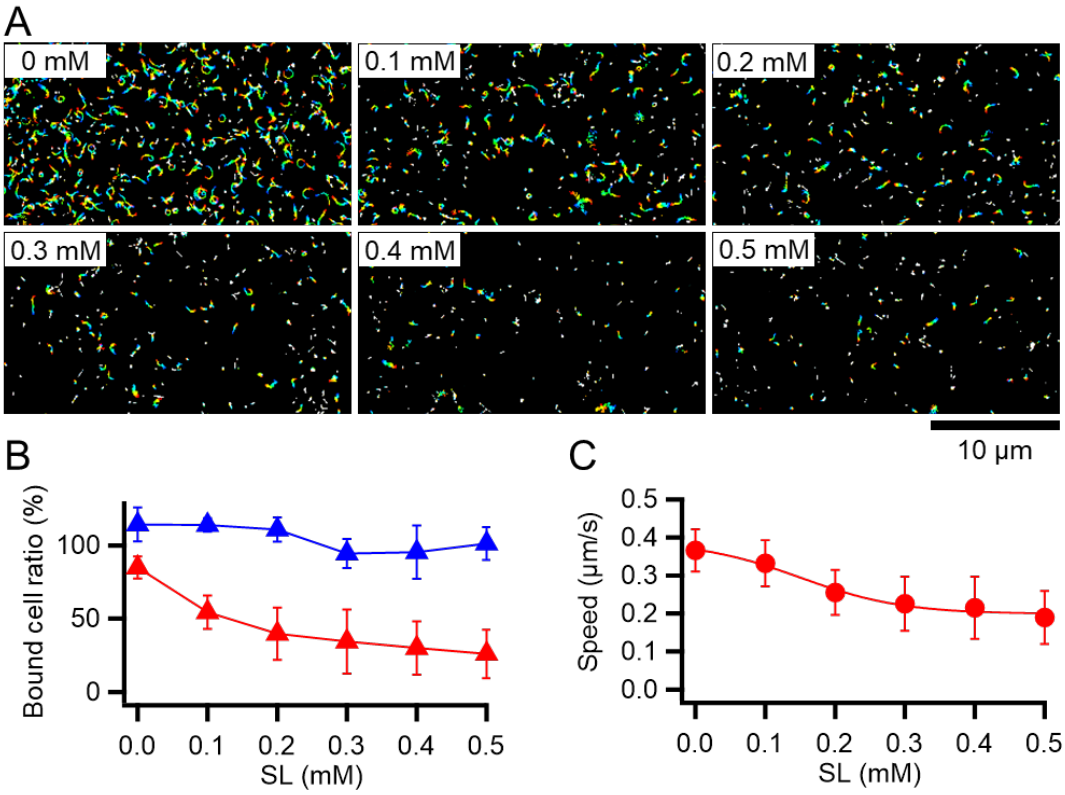

Figure 4. Effects of SL on binding and gliding. (A) Gliding cells were treated with free SL. The cell trajectories after SL treatment are presented as a stack for 20 s, changing color from red to blue. SL concentrations are shown at the left upper corner of each panel. (B) Number of cells bound to the glass at 5 min after treatment are plotted relative to the initial cell number. The averages for gliding (red triangles) and non-gliding (blue triangles) cells are shown with the standard deviations (n = 10, 10, 10, 10, 9, and 10 for 0, 0.1, 0.2, 0.3, 0.4, and 0.5 mM, respectively). (C) Averaged gliding speeds under various SL concentrations are plotted with the standard deviations and fitted by a sigmoidal curve (n = 50, 50, 50, 50, 56, and 56 for 0, 0.1, 0.2, 0.3, 0.4, and 0.5 mM, respectively).

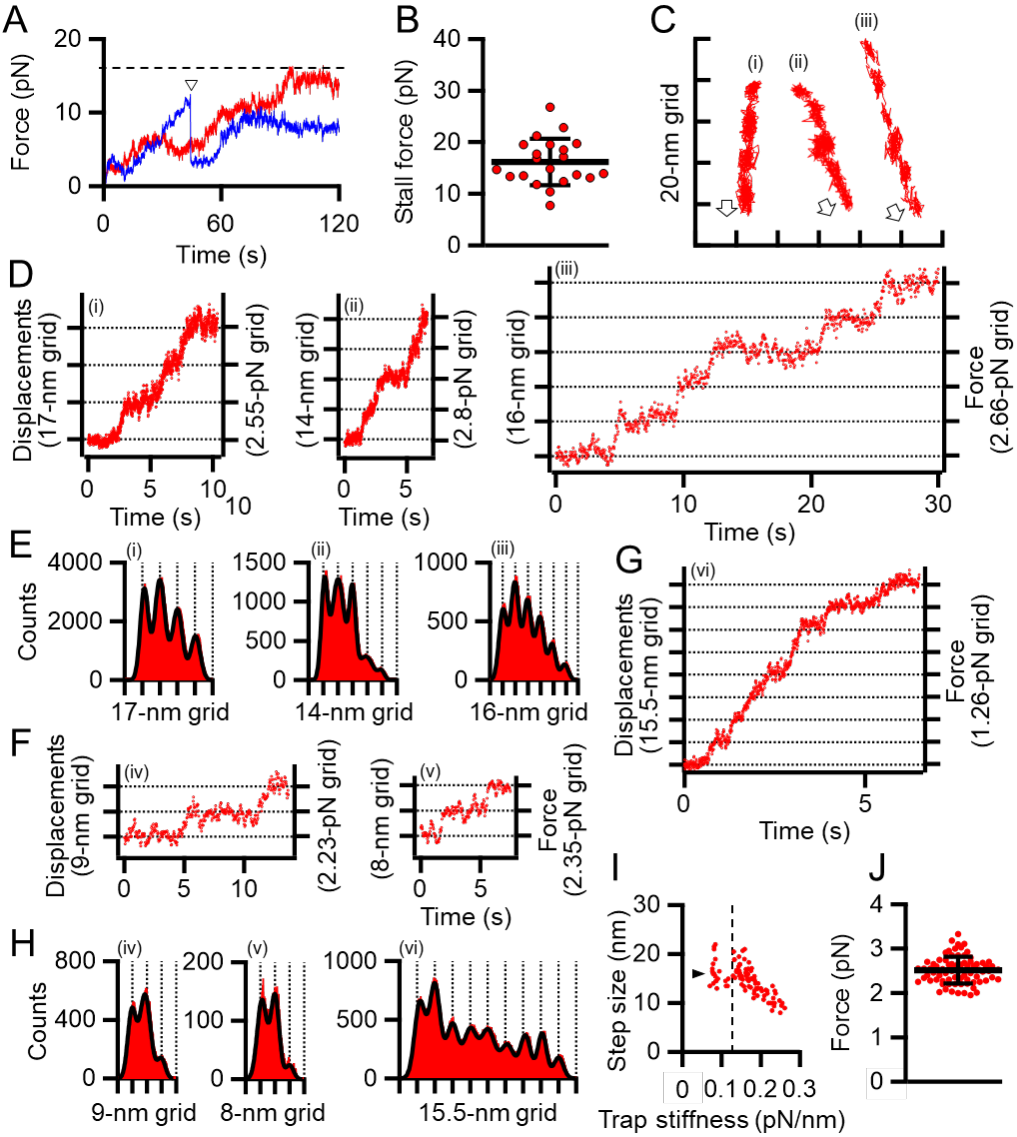

Figure 5. Stepwise movements under SL. (A) Representative force traces with time under 0.2–0.3 mM SL are shown for stalled (red) and detached (blue) cells. The broken line indicates the stall force. The time point of detachment is marked by a triangle. (B) Scatter dot plot of stall force shown with averages (thick line) and standard deviations (thin lines) (n = 21). (C) Three cell trajectories with stepwise movements are shown in a field. Open arrows indicate the gliding direction. (D) Displacement and force of cells whose trajectories are shown in panel (C). (E) Histograms of pairwise distance function (PDF) analysis of panel (D) were fitted by the sum of Gaussian curves. (F) Displacement and force under high trap stiffness. (G) Displacement and force under low trap stiffness. (H) Histograms of PDF analysis of panel (F) and (G). (I) Distribution of step size under various trap stiffnesses. Step sizes were plotted as a function of trap stiffness (n = 97). The position at 0.12 pN/nm of trap stiffness was marked by a dotted line. The average of step size under 0.07–0.12 pN/nm of trap stiffness was marked by a triangle. (J) Scatter dot plot of force increments under 0.13–0.26 pN/nm of trap stiffness shown with averages (thick line) and standard deviations (thin lines) (n = 76).

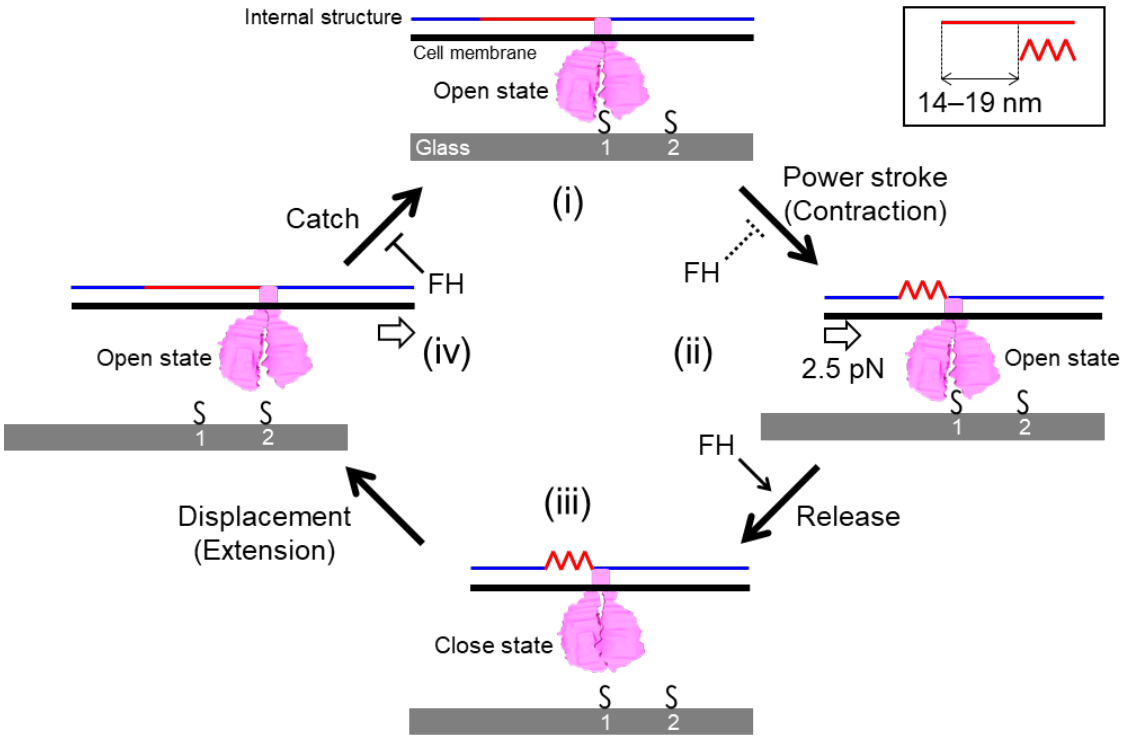

583

584

585 **Figure 6. Schematic illustration of leg behaviors in stepwise movements.** Internal structure,
586 represented by blue and red lines, is responsible for force transmission. It repeats contraction and
587 extension cooperatively with the surface structures. Conformational change of internal structure
588 and step size are shown in the right-upper box. GPCA is presented in pink. Sialylated
589 oligosaccharides are shown by "S." Force exerted in a step is shown by an arrow in panel (ii).
590 Displacement of the cell body forward is shown by an arrow in panel (iv). The gliding occurs
591 through stages i to iv. See text for details.
592